

# In Situ Vesicle Formation by a Kinetic Reaction in Aqueous Mixtures of Single-Tailed Catanionic Surfactants

Jingcheng Hao,<sup>\*,†,‡,§</sup> Zaiwu Yuan,<sup>†</sup> Weimin Liu,<sup>\*,‡</sup> and Heinz Hoffmann<sup>\*,§</sup>

Key Laboratory for Colloid and Interface Chemistry (Shandong University), Ministry of Education, Jinan 250100, P. R. China, State Key Laboratory of Solid Lubrication, Lanzhou Institute of Chemical Physics, Chinese Academy of Sciences, Lanzhou 730000, P. R. China, and Physikalische Chemie I, Universität Bayreuth, D-95440 Bayreuth, Germany

Received: December 9, 2003; In Final Form: February 19, 2004

Is the vesicle phase the spontaneous formation and the thermodynamically stable state? We answer the question by developing extremely dilute cationic and anionic (catanionic) aqueous mixtures of single-tailed surfactants in situ by designing a chemical reaction without shear forces. It is demonstrated that vesicles do spontaneously form in extremely dilute catanionic surfactant systems if one of the components is produced by a chemical reaction and not by mixing of the components which avoids the influence of shear-stress forces as previously described. The results in extremely dilute solutions are compared to those of our previous results in concentrated solutions, which clearly demonstrate that the final state (vesicle phase) at lower concentration is history independent at equilibrium. It is concluded that catanionic surfactant vesicle formation is produced spontaneously in extremely dilute solutions (water-rich), and the resultant vesicle phase is a thermodynamically stable state. In concentrated solutions, however, vesicle formation is not produced spontaneously, which means the shearing forces might be responsible for the formation of vesicles as a result of the external input of energy.

## Introduction

It is now well established that vesicles can be formed in aqueous solutions from single-chain surfactants by mixing various surfactants or surfactants with cosurfactants. One of the general methods is the combination of mixing cationic with anionic surfactants in aqueous solutions, which was published in the pioneering study by Kaler et al.<sup>1</sup> Their results showed that vesicles in aqueous mixtures of cationic/anionic surfactants of sufficient single-tailed chain length spontaneously form and are thermodynamically stable when the components are mixed. Besides Kaler et al.'s pioneering study<sup>1</sup> and their subsequent publications,<sup>2–6</sup> Zemb et al.,<sup>7–10</sup> Khan et al.,<sup>11–15</sup> Hoffmann et al.,<sup>16,17</sup> and others<sup>18–20</sup> conducted investigations on vesicles or other structures in catanionic surfactant mixtures both on experimental<sup>1–19</sup> and theoretical<sup>21–23</sup> grounds. However, the spontaneous formation and thermodynamic stability of vesicles are still under discussion.<sup>24,25</sup> In our previous investigations on single-tailed catanionic surfactant systems with a total surfactant concentration of 100 mM, we tried to develop special kinetic routes to build up the defined suspensions of multilamellar, onion-like vesicles<sup>26–29</sup> but obtained the stacked bilayer  $L\alpha$ -phase in aqueous mixtures of single-tailed catanionic surfactants. It was demonstrated that the final morphological state of a prepared phase depends on the route in which this phase is prepared. It was shown that a vesicle phase is obtained when a cationic surfactant solution was simply mixed with an anionic surfactant solution, whereas a stacked  $L\alpha$ -phase is obtained when the cationic component was produced by a chemical

reaction in the stagnant anionic surfactant solution. The final composition in the two differently prepared phases was the same. It thus became obvious that the route of preparation of the phase is of importance for the morphology of the final phase. The results clearly demonstrated that vesicles in concentrated aqueous mixtures of cationic/anionic surfactants are not formed spontaneously. This may be the result of shear forces that occur during the mixing process of the two components. The kinetically produced  $L\alpha$ -phase without shear forces is a classic  $L\alpha$ -phase with stacked bilayers which can be transferred into vesicles by shear forces that are turned upside down a few times, even though that does not give any quantitative measurement of how much shear had been given. It is therefore conceivable that the vesicles were not produced by the thermodynamic conditions in single-tailed catanionic surfactant systems, but the shear that was due to the mixing, that is, the shearing forces, might be responsible for the formation of vesicles. It is also shown that the  $L\alpha$ -phase can exist in two different states: the classic state with stacked bilayers and the vesicle state. Both states are stable for long times; however, it is believed that the classic state is the one which is in thermodynamic equilibrium. These papers thus gave the impression that in most preparations of vesicles shear-stress forces are the dominant factor, and not so much the thermodynamic equilibrium conditions.

In this present extension of work published previously,<sup>26–29</sup> we would like to point out that the situation is even more complicated. We would like to demonstrate that vesicles can also be prepared on the same system by kinetic reactions if only the concentrations are lowered. It is believed that the true spontaneous vesicles form by developing the extremely dilute catanionic surfactant mixtures without any shear forces, which means the resultant vesicle phase is a thermodynamically stable state. In order to carry out the research objectives, we used new

\* To whom correspondence should be addressed. Phone: +86-531-8366074(o). Fax: +86-531-8564750(o). E-mail: jhao@sdu.edu.cn.

<sup>†</sup> Shandong University.

<sup>‡</sup> Lanzhou Institute.

<sup>§</sup> Universität Bayreuth.

experimental techniques such as small-angle neutron scattering (SANS), electron spin resonance (ESR), and dynamic laser light scattering (DLLS) to study the extremely dilute kinetically produced cationic single-tailed surfactant system in situ; the spontaneous vesicles were obtained without shear forces, which means the vesicles could be prepared by chemical reactions.

## Experimental Section

**Chemicals.** The tetradecyldimethylamine oxide ( $C_{14}$ DMAO) was a gift from Clariant AG Gendorf (Frankfurt Am Main, Germany) and was delivered as a 25% solution. It was crystallized twice from acetone and characterized by melting point ( $130.2$  to  $\sim 130.5$  °C) and CMC ( $1.4 \times 10^{-4}$  M). The sodium dodecylethoxysulfate [ $CH_3(CH_2)_{11}(CH_2CH_2O)_{2.5}SO_3Na$ , Texapon N<sub>70</sub>] was a gift from Henkel (Düsseldorf, Germany) and was used without further purification. Methylformate ( $HCOOCH_3$ ) and 1.0 M formic acid ( $HCOOH$ ) solution from Merck were both P. A. quality. 5-Doxyl stearic acid, chosen as the spin probe in the electron spin resonance (ESR) measurements, was obtained from Sigma Chemical Co.  $D_2O$  (99.8% isotropic purity) used for the SANS experiments was obtained from Euriso-top, Groupe CEA, Saint Aubin (France), and water was doubly distilled.

**Phase Diagrams.** On the basis of observations collected on more than 250 samples with total different surfactant compositions of  $0.1\% < C_{total} < 3.0\%$  after equilibration for at least 4 weeks, the phase diagram of  $C_{14}$ DMAO– $HCOOH$  (1:1)/Texapon N<sub>70</sub>/water at  $25.00 \pm 0.05$  °C, in the region of the water-rich corner, was established. Phase boundaries were delineated based on visual observations of phase boundaries, which remained unchanged over an extended period of time, and were also carefully determined by conductivity measurements. The total samples were heated to  $\sim 50$  °C and kept for 4 weeks for equilibration at  $50.00 \pm 0.05$  °C. The phase diagram at  $50.00 \pm 0.05$  °C was drawn.

**Conductivity Measurements.** The conductivity measurements were performed on a “microprocessor conductivity meter” LF 2500 CON of WTW (Germany). The samples of  $L_1/L\alpha$ -phase,  $L\alpha$ /precipitate, and  $L_1/L\alpha$ -phase/precipitate were stirred during the conductivity measurements.

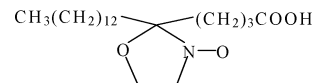
**Turbidity Measurements.** Turbidimetric measurements of the cationic/anionic  $L\alpha$ -phase solutions were carried out using a UV–vis–NIR spectrophotometer U-4100 at a constant wavelength of 360 nm. Absorbance was measured at  $\sim 25$  °C under constant-stirring conditions ( $\sim 100$  rpm) keeping the solutions in a temperature-controlled cell holder.

**DSC Measurements.** For the differential scanning calorimetry (DSC) measurements, a “MICRO-DSC” from Setaram (France) was employed. The samples with precipitates at  $25.00 \pm 0.05$  °C were completely stirred and transferred into aluminum pans. As reference a sealed pan with a corresponding amount of water was used. To check water evaporation, the pans were weighed before and after the DSC measurements. The DSC thermograms were recorded in the temperature range from 0 to more than 65 °C.

**SANS Measurements.** The small-angle neutron scattering (SANS) experiments were performed at the Hahn–Meitner Institute, Berlin (Germany), on the V4 instrument.<sup>30</sup> A wavelength of 6.0 Å was chosen, and sample-to-detector distances of 1, 4, and 15.85 m were employed. The data were recorded on a  $64 \times 64$  two-dimensional detector. They were afterward radially averaged and converted into absolute units, that is, the differential cross section, by comparison with the scattering of

a  $H_2O$  standard and proper correction for detector background and the scattering of the empty cell.<sup>31,32</sup>

**ESR Measurements.** A stock solution ( $2.0 \times 10^{-3}$  mol·L<sup>-1</sup>) of 5-doxyl stearic acid



was prepared with ethanol. 100  $\mu$ L of probe solution was injected into a 1 mL graduated tube, and the films of 5-doxyl stearic acid were generated in a nitrogen atmosphere by evaporation. Then the sample solution to be measured was injected into the tube; the final probe concentration was  $2.0 \times 10^{-4}$  mol·L<sup>-1</sup>. ESR measurements were performed with an E-115 spectrometer operating in the X-band. The correlation times ( $\tau_c$ ) for the probe motion have been computed using the following equation:<sup>33</sup>

$$\tau_c = 6.5 \times 10^{-10} \Delta H_0 [(h_0/h_{-1})^{1/2} + (h_0/h_{+1})^{1/2} - 2] \quad (1)$$

where  $\Delta H_0$  and  $h_0$  are the line width and the height of the central-field peak, respectively,  $h_{-1}$  is the height of the high-field peak, and  $h_{+1}$  is the height of the low-field peak.

**DLS Measurements.** To prepare dust-free solutions for dynamic light-scattering (DLS) measurements, the sample solutions were filtered directly into dust-free light-scattering cells through a Millipore sterile membrane filter depending on the concentrations and the sizes of the aggregates. The light-scattering cells had been rinsed inside and outside with distilled (dust-free) acetone to ensure a dust-free condition before use. A standard laboratory-built laser light-scattering spectrometer equipped with a Coherent Radiation 200 mW diode pumped solid-state (DPSS) 532 laser, operating at 532 nm, and a Brookhaven Instruments (BI-9000AT) correlator was used for the DLS measurements. The spectrometer is capable of making measurements of both the angular dependence of the absolute integrated scattered intensity over a scattering angular range from 20° to 140° and of intensity–intensity digital photon correlation over a similar angular range (DLS and depolarized DLS). About 2 to  $\sim 3$  mL of sample solution was transferred into a special dust-free light-scattering cell for light-scattering measurements. The scattering cells were held in a brass thermostat block filled with refractive-index-matching silicone oil. The temperature was controlled to within  $\pm 0.05$  °C.

Dynamic light scattering (DLS) measures the intensity–intensity time correlation function  $G^{(2)}(\Gamma)$  in the self-beating mode where  $\Gamma$  is the characteristic line width. The  $G^{(2)}(\Gamma)$  can be related to the electric field time correlation function  $g^{(1)}(\tau)$  as follows:

$$G^{(2)}(\Gamma) = A(1 + b|g^{(1)}(\tau)|^2) \quad (2)$$

where  $A$  and  $b$  are, respectively, the background (baseline) and a coherence factor (a parameter depending on the detection coherence). The electric field time correlation function,  $|g^{(1)}(\tau)|$ , was analyzed by the constrained regularized CONTIN method,<sup>34,35</sup> to yield the characteristic line width distribution  $G(\Gamma)$  by inversion of

$$|g^{(1)}(\tau)| = \int_0^\infty G(\Gamma) e^{-\Gamma\tau} d\Gamma \quad (3)$$

The first and second moments of  $G(\Gamma)$  are  $\langle \Gamma \rangle = \int_0^\infty \Gamma G(\Gamma) d\Gamma$  and  $\mu_2 = \int_0^\infty (\Gamma - \langle \Gamma \rangle)^2 G(\Gamma) d\Gamma$ , respectively. The value of

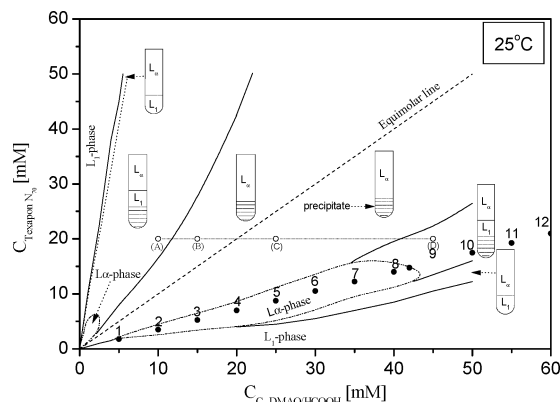


**Figure 1.** Phase diagram of  $C_{14}$ DMAO-HCOOH (1:1)/Texapon N<sub>70</sub>/water in the region of the water-rich corner,  $T = 25.00 \pm 0.05$  °C.

$\mu_2/\langle\Gamma\rangle^2$  is a measure of the particle polydispersity. If the relaxation is diffusive,  $\Gamma$  can be related to the average apparent diffusion coefficient ( $D$ ):

$$D = \Gamma/q^2 \quad (4)$$

The apparent hydrodynamic radius,  $R_h$ , can be obtained via the Stokes-Einstein equation:

$$R_h = k_B T / 6\pi\eta D \quad (5)$$

where  $k_B$  is the Boltzmann constant and  $\eta$  is the solvent viscosity at temperature  $T$ . On the basis of eqs 4 and 5, a characteristic line width distribution  $G(\Gamma)$  corresponds to a distribution of an apparent hydrodynamic radii from which, for example, the average apparent hydrodynamic radius  $R_h$  can be determined. The DLS measurements were performed at finite concentrations and interparticle interactions have been neglected.

**FF-TEM Images.** The microstructures of the samples with the birefringence between the polarizers were examined by FF-TEM (freeze-fracture transmission electron microscopy) images. A small amount of sample ( $\sim 4$   $\mu$ L) was placed on a 0.1 mm thick copper disk covered with a second copper disk. The copper sandwich with the sample was frozen by plunging this sandwich into liquid propane which had been cooled by liquid nitrogen. For fracturing and replication a freeze-fracture apparatus (Balzer BAF 400, Germany) was used at a temperature of  $-140$  °C. Pt/C was deposited at an angle of  $45^\circ$ . The replicas were examined with a Zeiss CEM 902 transmission electron microscope operated at 80 kV. In order to avoid the external shear forces during the sample preparation from the rapid freezing, the  $L_1$ -phase mixed with methylformate was filled between the copper sandwich and the chemical reaction occurred in the sandwich. After the reaction was completed, the sample was plunged into liquid propane and a replica was prepared.

All the experiments described in the following discussion were done at  $25.00 \pm 0.05$  °C unless specified otherwise.

## Results and Discussion

**Part I.  $C_{14}$ DMAO-HCOOH (1:1)/Texapon N<sub>70</sub>/Water Catanionic System.** *I.1. Phase Diagram of  $C_{14}$ DMAO-HCOOH (1:1)/Texapon N<sub>70</sub>/Water at the Water-Rich Corner at 25 °C.* On the basis of observations collected on more than 250 samples after equilibration for at least 4 weeks with different compositions ( $0.1\% < c_{\text{total}} < 3.0\%$ ), the phase diagram of  $C_{14}$ DMAO-HCOOH(1:1)/Texapon N<sub>70</sub>/water at  $25.00 \pm 0.05$  °C at atmospheric condition, in the region of the water-rich corner, was established and is depicted in Figure 1. Phase boundaries

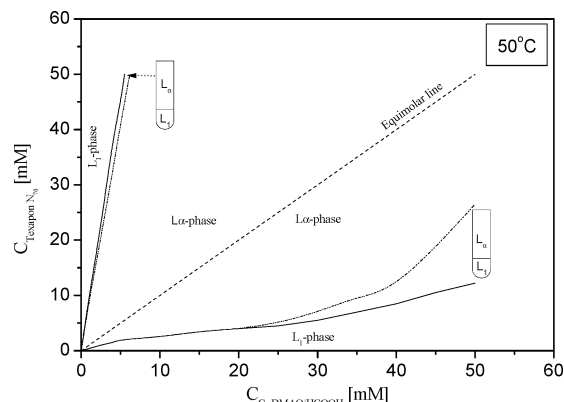
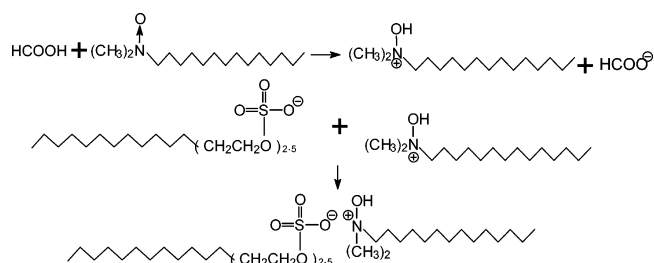


**Figure 2.** Phase diagram of  $C_{14}$ DMAO-HCOOH (1:1)/Texapon N<sub>70</sub>/water in the region of the water-rich corner,  $T = 25.00 \pm 0.05$  °C.

were delineated after visual observations remained unchanged over an extended period of time and were also carefully determined by conductivity measurements. Using electrical conductivity measurements, we were able to distinguish the  $L_1$ , vesicle ( $L_\alpha$ -phase),  $L_1/L_\alpha$ -phase,  $L_\alpha$ /precipitate, and  $L_1/L_\alpha$ -phase/precipitate regions. The  $L_\alpha$ -phase solutions in the cationic  $C_{14}$ DMAOH<sup>+</sup>-rich side are turbid and slightly bluish and when strongly turned between crossed polarizers yield the very weak birefringence. The  $L_\alpha$ -phase region has a concentration range of  $\sim 0.1\%$  ( $\sim 5$  mM)  $< c_{C_{14}DMAO} < \sim 1.0\%$  ( $\sim 43$  mM) and  $\sim 0.1\%$  ( $\sim 3$  mM)  $< c_{\text{Texapon N70}} < \sim 0.5\%$  ( $\sim 15$  mM). In the mixed solutions of  $C_{14}$ DMAO-HCOOH (1:1)/Texapon N<sub>70</sub>/water, the zwitterionic surfactant  $C_{14}$ DMAO should be charged by formic acid to the cationic surfactant,  $C_{14}$ DMAOH<sup>+</sup>, which then reacts with the cationic and anionic surfactant combination. In this route, the system has excess sodium formate. The reaction is as follows:



*I.2. Temperature-Induced Precipitate Phase into the  $L_\alpha$ -Phase.* The samples with precipitate at 25 °C are very interesting. When heated, the precipitate dissolves above 35 °C. It could transfer to the neighbor single  $L_\alpha$ -phase. The phase diagram of  $C_{14}$ DMAO-HCOOH (1:1)/Texapon N<sub>70</sub>/water at 50 °C, in the region of the water-rich corner, was established, and is shown in Figure 2. The dissolution temperature of the precipitate was detected by differential scanning calorimetry (DSC) measurements. The DSC measurement results are shown in Figure 3, in which the compositions used for DSC measurements are shown in Figure 1 (A,  $L_1/L_\alpha$ -phase/precipitate; B,  $L_\alpha$ -phase/precipitate; C,  $L_\alpha$ -phase/precipitate; D,  $L_1/L_\alpha$ -phase/precipitate). One can easily see the phase transition peaks at about 35 °C, which means that at temperatures lower than 35 °C the cationic/anionic surfactant precipitate is formed. All the phase separation samples with precipitate (two or three phases) could be transformed into the single  $L_\alpha$ -phase at about 35 °C, independent of the compositions.

*I.3. Conductivity Data.* The phase diagram was delineated based on visual observations of phase boundaries, which

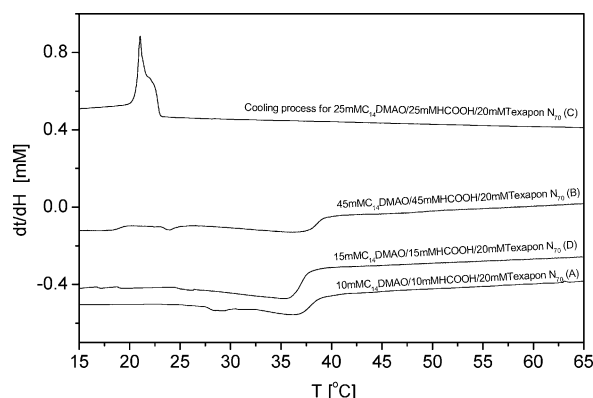


**Figure 3.** DSC data of different compositions as indicated in Figure 1. The different phase regions are as follows: A,  $L_1/L\alpha$ -phase/precipitate; B,  $L\alpha$ -phase/precipitate; C,  $L\alpha$ -phase/precipitate; D,  $L_1/L\alpha$ -phase/precipitate. At temperatures lower than 35 °C a precipitate is formed.

remained unchanged over an extended period of time and was also carefully determined by conductivity measurements. Using electrical conductivity measurements, we were able to distinguish the  $L_1$ ,  $L\alpha$ -phase,  $L_1/L\alpha$ -phase,  $L\alpha$ /precipitate, and  $L_1/L\alpha$ -phase/precipitate regions. The conductivity data are shown in Figure 4, where 10 mM  $C_{14}$ DMAO–HCOOH(1:1), 20 mM  $C_{14}$ DMAO–HCOOH(1:1), 30 mM  $C_{14}$ DMAO–HCOOH(1:1), and 35 mM  $C_{14}$ DMAO–HCOOH(1:1) were chosen as the measurement routes. The conductivity data are plotted against the variable Texapon  $N_{70}$  concentrations. The phase boundaries were well determined by the conductivity data. For example,

at a constant 30 mM  $C_{14}$ DMAO–30 mM HCOOH, with increasing Texapon  $N_{70}$  we observe an  $L_1$ -phase, a two-phase  $L_1/L\alpha$ -region where the low-birefringent  $L\alpha$ -phase is on the top of the samples, then after the two-phase region we find a single low-birefringent  $L\alpha$ -phase, and finally at almost equal mole fraction a precipitate is formed.

**1.4. Conductivity in the  $L\alpha$ -Phase and  $L_1$ -Phase/ $L\alpha$ -Phase/Precipitate Regions and the Relative Turbidity and Viscosity of the  $L\alpha$ -Phase Region.** The  $L\alpha$ -phase solutions in the cationic  $C_{14}$ DMAOH<sup>+</sup>-rich side are very stable, slightly turbid, and less bluish. The  $L\alpha$ -phase could be transferred into other phases when the cationic/anionic surfactant ratios change.  $L\alpha$ -phase sample solutions have interesting conductivity, relative turbidity, and viscosity properties with the change of compositions. We chose the different compositions indicated in Figure 1 (from 1 to 12) to study the interesting properties of the  $L\alpha$ -phase and  $L_1$ -phase/ $L\alpha$ -phase/precipitate regions, where the compositions chosen pass through the  $L\alpha$ -phase and  $L_1$ -phase/ $L\alpha$ -phase/precipitate regions. The conductivity measurements in the  $L\alpha$ -phase and  $L_1$ -phase/ $L\alpha$ -phase/precipitate regions were carried out at  $25.00 \pm 0.05$  °C, and the sample solutions were stirred when the conductivity was measured. The results are shown in Figure 5. From the conductivity data, one can see that the conductivity increases linearly with the total surfactant concentrations in the  $L\alpha$ -phase region, and the phase transition occurs at about  $\sim 15$  mM Texapon  $N_{70}$ /40 mM  $C_{14}$ DMAO–HCOOH (1:1), which was observed from the phase diagram where the  $L\alpha$ -phase transfers to  $L_1$ -phase/ $L\alpha$ -phase/precipitate. The viscosity and turbidity data in the  $L\alpha$ -phase regions were deter-

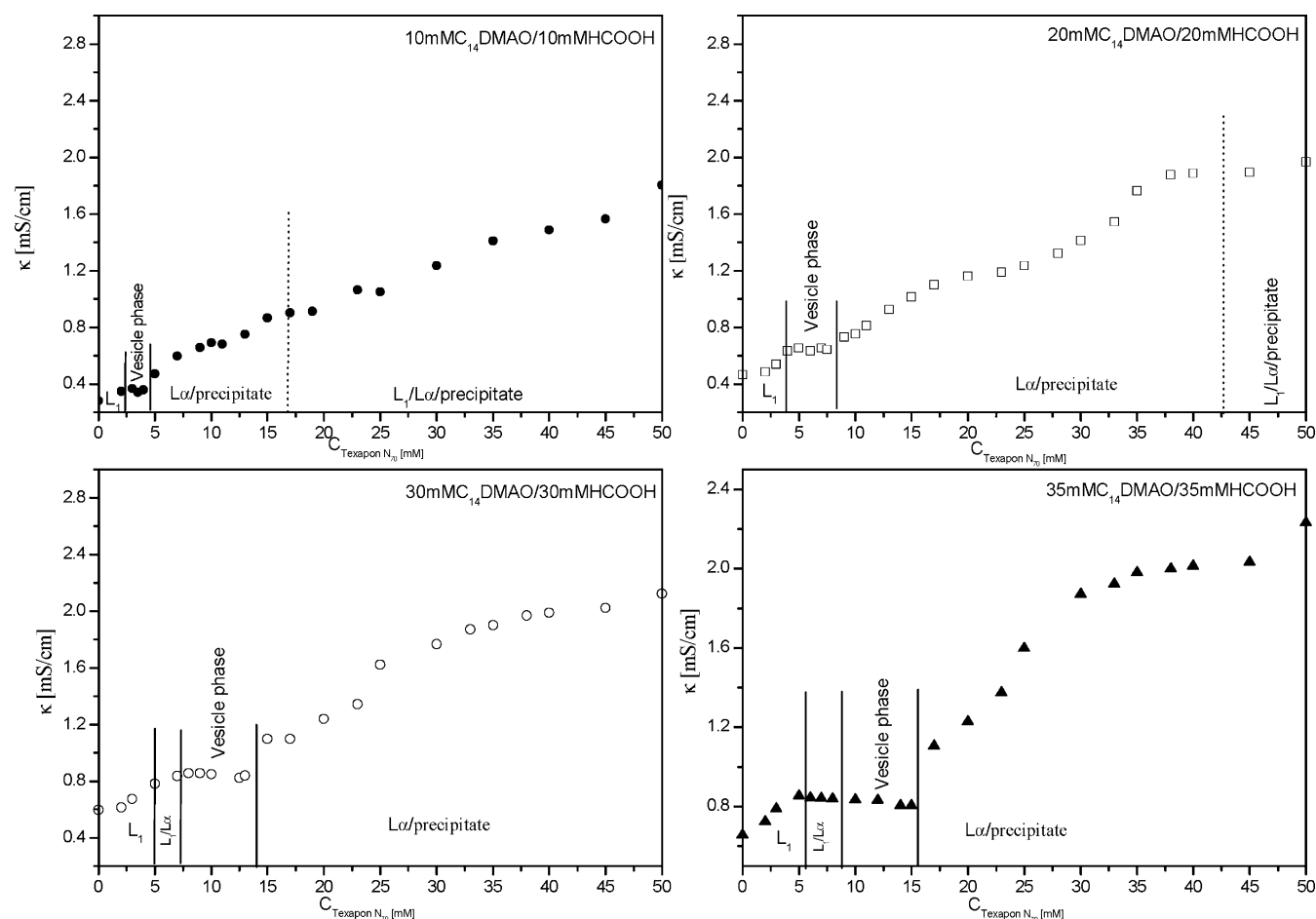


**Figure 4.** Phase boundaries determined by conductivity data. The routes chosen to measure conductivity are 10 mM  $C_{14}$ DMAO–HCOOH (1:1), 20 mM  $C_{14}$ DMAO–HCOOH (1:1), 30 mM  $C_{14}$ DMAO–HCOOH (1:1), and 35 mM  $C_{14}$ DMAO–HCOOH (1:1).



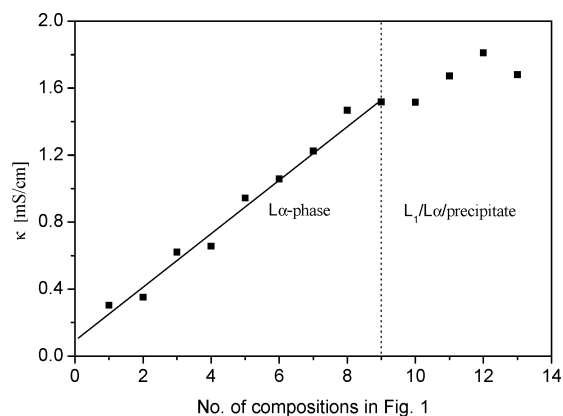


**Figure 5.** Conductivity data in the  $L\alpha$ -phase and  $L_1$ -phase/ $L\alpha$ -phase/precipitate.

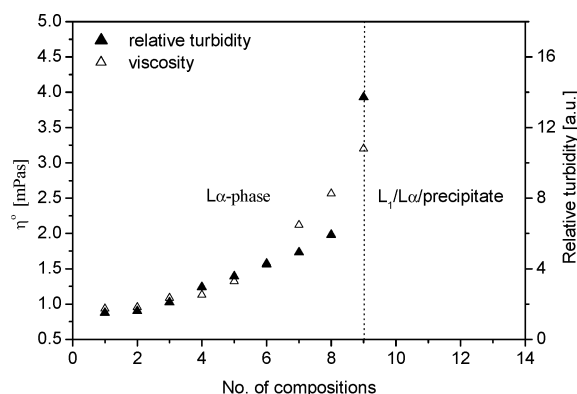


**Figure 6.** Viscosity and relative turbidity data in the  $L\alpha$ -phase.

mined, and are shown in Figure 6. In the  $L\alpha$ -phase region, one can see that the viscosity and turbidity increase with the total surfactant concentrations.

**1.5. FF-TEM Images of the  $L\alpha$ -Phase.** The microstructures of the  $L\alpha$ -phase in the  $C_{14}$ DMAOH<sup>+</sup>-rich side were determined by FF-TEM. The slightly bluish, low viscosity, and isotropic  $L\alpha$ -phase contains vesicles. A typical FF-TEM micrograph of a  $C_{14}$ DMAOH<sup>+</sup>-rich  $L\alpha$ -phase sample with 30 mM  $C_{14}$ -DMAO-HCOOH (1:1)/10.5 mM Texapon N<sub>70</sub>/water is shown in Figure 7. The features of the vesicles are apparent: (i) both unilamellar and multilamellar vesicles coexist, which is different from the observation of Kaler et al.<sup>1</sup> where they only observed the uniformly unilamellar vesicles throughout the samples both in cationic-rich and anionic-rich samples; (ii) both unilamellar and multilamellar vesicles have rather polydispersed size distributions. The unilamellar vesicles have diameters ranging from about 20 nm to more than 500 nm, and the multilamellar vesicles have diameters ranging from about 500 nm to 4.5  $\mu$ m; (iii) the large multilamellar vesicles are relatively rarely present; (iv) in the multilamellar vesicles, the interlamellar spacing between two adjacent bilayers is about 100 nm.

**Part II. In Situ Vesicle Formation by a Kinetic Reaction in Aqueous Mixtures of Single-Tailed Catanionic Surfactants.** In part I, we studied the microstructures and the properties of the  $C_{14}$ DMAO-HCOOH (1:1)/Texapon N<sub>70</sub>/water system at the water-rich corner. The FF-TEM image clearly shows that the vesicles are formed when one prepares the cationic/anionic surfactant aqueous solutions. The results on spontaneous vesicle formation in the catanionic surfactant aqueous mixtures are consistent with those observations.<sup>1</sup>

In order to avoid external shear forces introduced by mixing, one kinetic route is used to produce the  $L\alpha$ -phase samples in

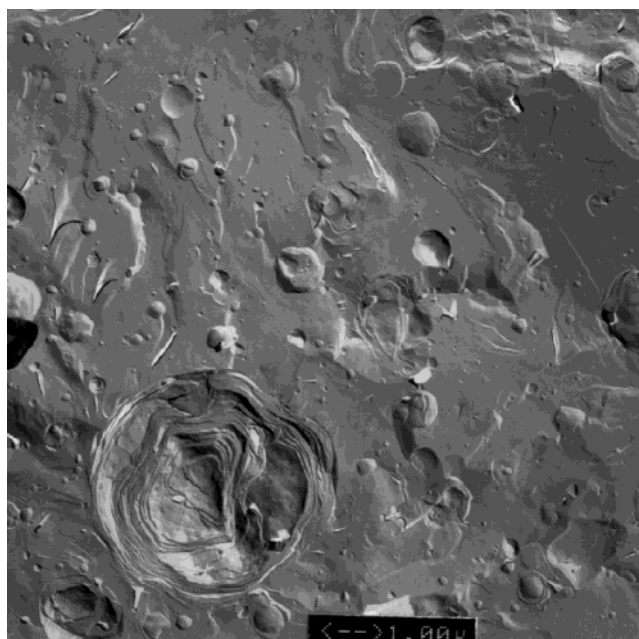


**Figure 7.** Typical FF-TEM image of vesicles in the  $C_{14}$ DMAOH<sup>+</sup>-rich side with 30 mM  $C_{14}$ DMAO-HCOOH (1:1)/10.5 mM Texapon N<sub>70</sub>/water. The bar represents 1.00  $\mu$ m.

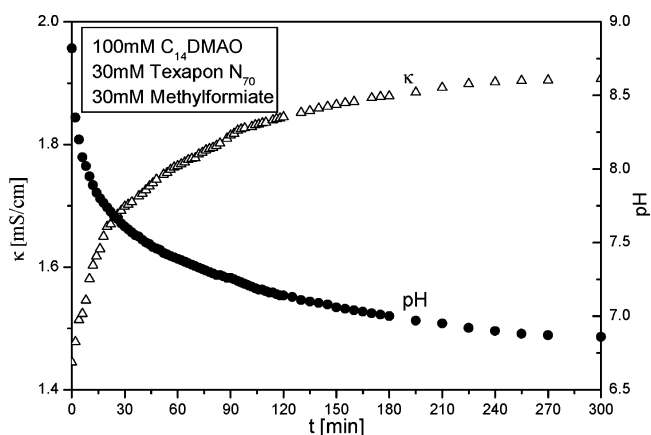


**Figure 8.** Decrease in pH and increase in conductivity of the solution as a function of time with the system 100 mM  $C_{14}$ DMAO, 30 mM Texapon N<sub>70</sub>, and 30 mM methylformiate.

the  $L_1$ -phase solutions in situ. The different compositions in the  $C_{14}$ DMAOH<sup>+</sup>-rich  $L\alpha$ -phase region chosen to prepare the  $L\alpha$ -phase samples by the kinetic route were (a) 10 mM  $C_{14}$ -DMAO-HCOOH/3.5 mM Texapon N<sub>70</sub>/water; (b) 20 mM  $C_{14}$ -DMAO-HCOOH/7.0 mM Texapon N<sub>70</sub>/water; and (c) 30 mM  $C_{14}$ -DMAO-HCOOH/10.5 mM Texapon N<sub>70</sub>/water. However, the precursor of HCOOH, methylformiate ( $HCOOCH_3$ ), was used instead of HCOOH.  $HCOOCH_3$  slowly hydrolyzed into formic acid and methanol. Methanol has hardly any effect on lyotropic mesophases.<sup>36</sup> The sample still remained as the  $L_1$ -phase when  $HCOOCH_3$  was added to reach the final concentration, such as  $c_{HCOOCH_3} = 20$  mM. It takes about 1 day to complete the hydrolysis of  $HCOOCH_3$ ; the process of the hydrolysis of methylformiate in the  $L_1$ -phase solution can be checked by measuring the pH and the conductivity. The decrease in pH and the increase in conductivity of the solution as a function of time are given in Figure 8.

In the next experiments, we used four techniques which do not input any external energy (without any disorder to the structures of the samples) to monitor the microstructures of two sample solutions. One sample labeled "A" is 20 mM  $C_{14}$ -

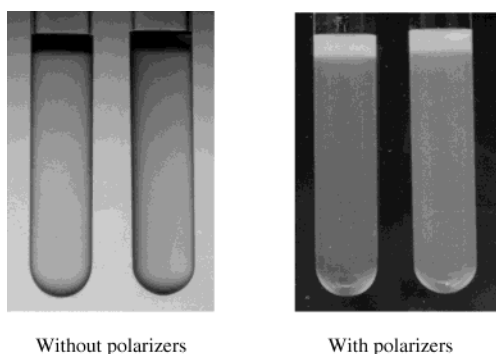


**Figure 9.**  $\alpha$ -phases: “A” after completion of the hydrolysis of methylformate at rest in 20 mM  $C_{14}$ DMAO/20 mM  $HCOOCH_3$ /7.0 mM Texapon  $N_{70}$ /water and “B” from the “A” sample by turning it upside down a few times. The “B” sample was kept at  $25.00 \pm 0.05$  °C for 4 weeks after being shaken by hand.

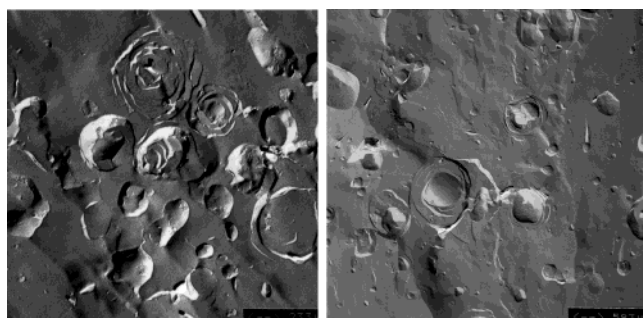


**Figure 10.** FF-TEM images of two samples: “A”, 20 mM  $C_{14}$ DMAO– $HCOOCH_3$  (1:1)/7.0 mM Texapon  $N_{70}$ /water after the completion hydrolysis at rest; “B”, from “A” by turning it upside down a few times. In the “A” sample (left image, the bar represents 0.233  $\mu$ m) the unilamellar vesicle diameters range from 30 to 500 nm and the multilamellar vesicle diameters are from 400 to 600 nm. In the “B” sample (right image, the bar represents 0.583  $\mu$ m) the unilamellar vesicle diameters range from 10 nm to about 100 nm and the multilamellar vesicle diameters are from 350 nm to more than 1.0  $\mu$ m.

DMAO– $HCOOCH_3$  (1:1)/7.0 mM Texapon  $N_{70}$ /water after completion of hydrolysis of methylformate at rest; another sample solution labeled “B” is made from the “A” sample by turning it upside down a few times, which means an input of external energy even though it does not give quantitative measurements of how much shear had been given. In Figure 9, two sample solutions of “A” and “B” are shown. From the two samples with or without polarizers, one cannot see the difference in the macroscopic properties. The  $\alpha$ -phase samples without shaking and with turning upside down a few times by hand show the slightly turbid and the less birefringent pattern which is typical for a multidomain situation. The two solutions seem to be obviously identical samples, which means the two samples have identical structures, which should be demonstrated by other experimental methods. We would like to point out that the two samples are stable for a long time (more than 2 years), and we did not observe any changes of macroscopic properties, which means the final samples with and without shaking are history independent at thermodynamic equilibrium.

Figure 10 shows the FF-TEM micrographs of the final sample “A” and the sample “B”. It clearly shows that both samples contain unilamellar and multilamellar vesicles similar to those in Figure 7, which means the same structures in the two samples exist and the structures do not depend on the external shear forces. This is the first time that true vesicles have been produced in situ by developing catanionic surfactant mixtures by a kinetic reaction.

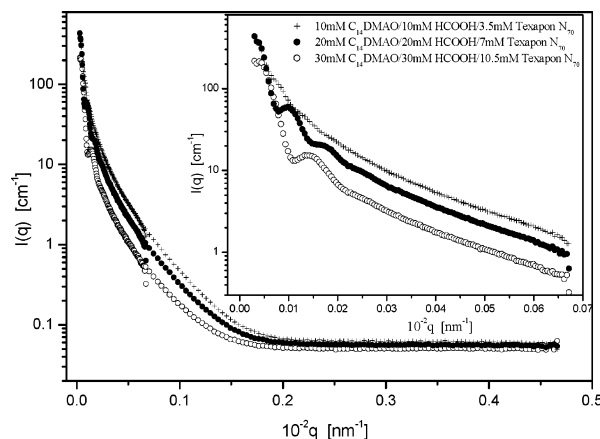


**Figure 11.** SANS intensity curves of three samples: (a) 10 mM  $C_{14}$ DMAO–10 mM  $HCOOCH_3$ /3.5 mM Texapon  $N_{70}$ /water; (b) 20 mM  $C_{14}$ DMAO–20 mM  $HCOOCH_3$ /7.0 mM Texapon  $N_{70}$ /water; (c) 30 mM  $C_{14}$ DMAO–30 mM  $HCOOCH_3$ /10.5 mM Texapon  $N_{70}$ /water. The three samples were prepared by chemical reaction at rest without shear forces.

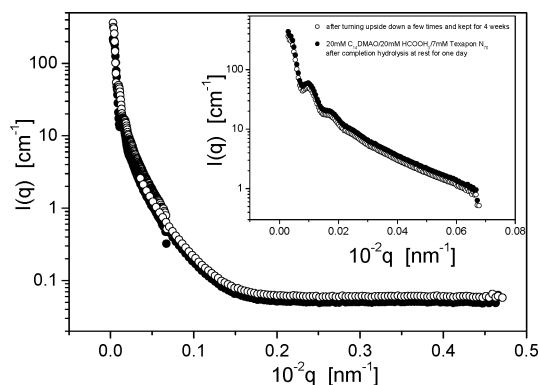


**Figure 12.** SANS curves from samples “A” and “B” (after turning upside down a few times and kept at  $25.00 \pm 0.05$  °C for 4 weeks). The same scattering curves mean the same structures exist in the two samples.

The SANS of three final samples after completion of  $HCOOCH_3$  hydrolysis (more than 1 day) at rest for different compositions chosen in the  $\alpha$ -phase region from Figure 1 were measured, where the compositions are (a) 10 mM  $C_{14}$ DMAO–10 mM  $HCOOCH_3$ /3.5 mM Texapon  $N_{70}$ /water, (b) 20 mM  $C_{14}$ DMAO–20 mM  $HCOOCH_3$ /7.0 mM Texapon  $N_{70}$ /water, and 30 mM  $C_{14}$ DMAO–30 mM  $HCOOCH_3$ /10.5 mM Texapon  $N_{70}$ /water. The SANS curves are shown in Figure 11. The curves showed the typical scattering behavior of  $\alpha$ -phase solutions with charged bilayers. We can easily obtain the interlamellar distance between the bilayers from the first and second maximum. The interlamellar scattering maximum gives an interlamellar distance of  $d = 2\pi/q_{\max} = \sim 130$  nm for 10 mM  $C_{14}$ DMAO–10 mM  $HCOOCH_3$ /3.5 mM Texapon  $N_{70}$ /water,  $\sim 64$  nm for 20 mM  $C_{14}$ DMAO–20 mM  $HCOOCH_3$ /7.0 mM Texapon  $N_{70}$ /water, and  $\sim 42$  nm for 30 mM  $C_{14}$ DMAO–30 mM  $HCOOCH_3$ /10.5 mM Texapon  $N_{70}$ /water. The interlamellar distance decreases with the total surfactant concentrations.

In order to monitor the structures in the two samples “A” and “B”, SANS measurements were carried out. The SANS results are shown in Figure 12. The scattering curves of the two samples are quite similar, which demonstrates that the microstructures in the two samples are the same. The interlamellar scattering maximum gives an interlamellar distance of  $d = 2\pi/q_{\max} = \sim 64$  nm and  $\sim 62$  nm for samples “A” and “B”, respectively.

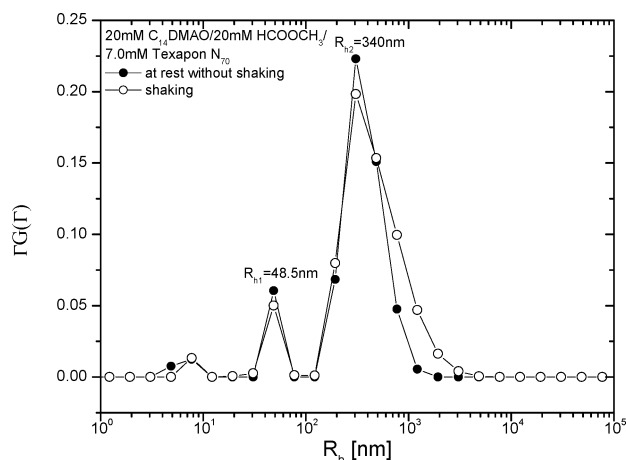


**Figure 13.** Apparent hydrodynamic radius distributions of the two samples "A" and "B".

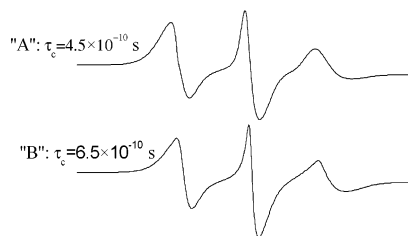


**Figure 14.** ESR spectra of the two samples "A" and "B".

The same structures exist in the two sample solutions, which could be demonstrated again by the DLS and ESR measurements. The two techniques are used to continuously monitor the kinetic hydrolysis of methylformate in the dilute solution

of 20 mM  $C_{14}$ DMAO–20 mM  $HCOOCH_3$ /7.0 mM Texapon  $N_{70}$ /water. The apparent hydrodynamic radius distributions and ESR spectra are shown in Figures 13 and 14.

From the CONTIN analysis of the two samples of "A" and "B" in Figure 13, one can see the similar phenomena as in the SANS measurements; the apparent hydrodynamic radius distributions of the two samples are astonishingly identical, which demonstrates that the same structures are present in the two solutions. Two different modes can be identified from the DLS results; the small and large aggregates have the  $R_h$  values of about 10 nm ( $R_{h1}$ ) and 48.5 nm ( $R_{h2}$ ), which correspond to the first and second peaks. We attribute the two peaks to the small and large unilamellar vesicles, respectively. The third peak at the  $R_{h3}$  value of around 340 nm could be attributed to the multilamellar vesicles.

We chose 5-doxyl stearic acid as the spin probe in the ESR measurements. The two ESR spectra (Figure 14) have quite the same spectral shape, and the high-field peaks for both samples are all wide. The correlation times,  $\tau_c = 6.5 \times 10^{10} \cdot \Delta H_0 [(h_0/h^{-1})^{1/2} + (h_0/h_{+1})^{1/2} - 2]$ ,<sup>33</sup> were calculated as  $4.5 \times 10^{-10}$  s and  $6.5 \times 10^{-10}$  s, respectively. The same ESR spectral shape and the similar  $\tau_c$  values show that the spin probe molecules are located in similar conformational environments in the two solutions of "A" and "B".

The phase transformation of the  $L_1$ -phase is completely interesting during the hydrolysis of methylformate in the  $C_{14}$ -DMAO and Texapon  $N_{70}$  mixed micellar aqueous solution. When  $C_{14}$ DMAO,  $HCOOCH_3$  and Texapon  $N_{70}$  are mixed, the isotropic, clear, and low viscosity  $L_1$ -phase was obtained. The solution remains in the  $L_1$ -phase state when methylformate is added to reach a concentration of 20 mM. Methylformate is a hydrophilic compound and solubilizes in the water domains of

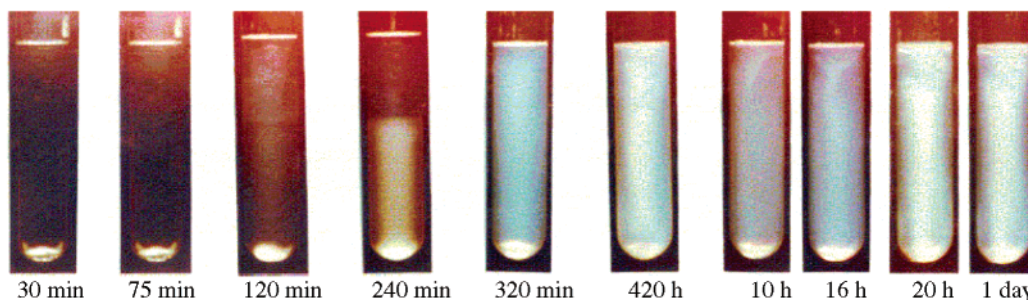


**Figure 15.** Series of different states of a sample to which 30mM of methylformate has been added to 100 mM of  $C_{14}$ DMAO and 30 mM of Texapon  $N_{70}$   $L_1$ -phase without stirring. Increasing time intervals have passed since the mixing, and observation is with crossed polarizers. In order to clearly observe the transformation of phases during the hydrolysis of methylformate, the total surfactant concentration is increased.

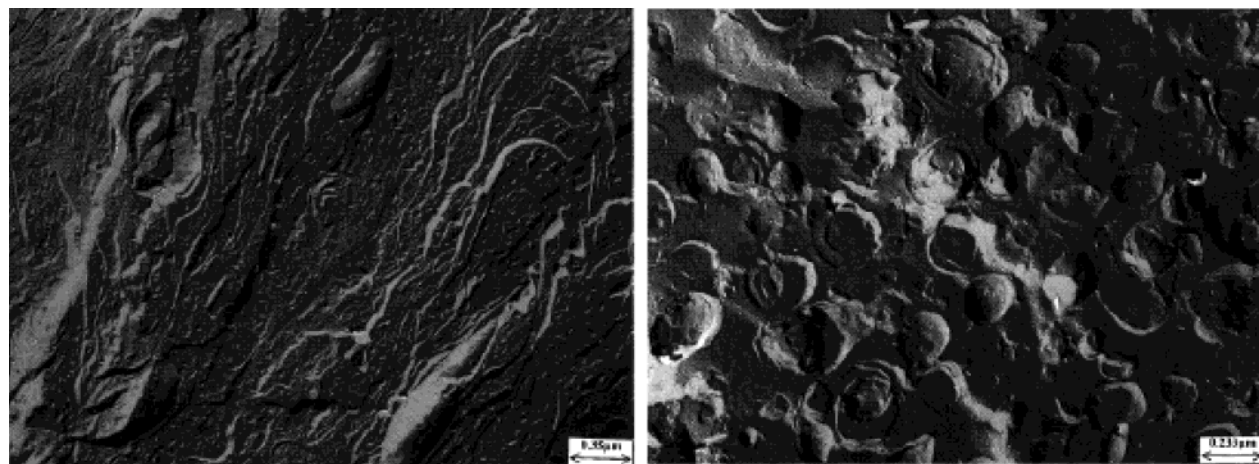


**Figure 16.** Freeze–fracture micrographs that were prepared from (a, left) a sample of 100 mM  $C_{14}$ DMAO, 30 mM Texapon  $N_{70}$ , and 30 mM methylformate after 1 day of hydrolysis without shearing and (b, right) the sample after 1 day of hydrolysis and shaking before measurement.



the mixed micellar solution. The DLS measurements just show small micelles at the beginning of methylformate addition by the CONTIN analysis (not shown). With increasing time, the sample develops into different phases and finally to the  $L\alpha$ -phase. In Figure 15, a series of different states of a sample are shown to which 30 mM methylformate was added and increasing time intervals had passed since the mixing. We notice that 45 min after the methylformate is added to the original  $L_1$ -phase the solution is still a low viscosity  $L_1$ -phase, then it develops into a viscous  $L_1$ -phase (<90 min), then into the two-phase  $L_1/L\alpha$  region where the birefringent  $L\alpha$ -phase is on the top of the sample (>120 min), and finally after more than 5 h it develops into the birefringent  $L\alpha$ -phase, which can easily be observed in the solution at rest between crossed polarizers. The birefringence domain pattern of the single  $L\alpha$ -phase does not change a lot with time. Even after 1 day the sample looks very much the same. We kept both samples at 25 °C for several months to look at their appearance with and without polarizers, we did not notice any change in the optical appearance of the two phases. The phase transformation experiment combined with the FF-TEM images, SANS, DLS, and ESR results unambiguously demonstrates that the final state that is reached after the completion of the hydrolysis without shaking at rest and with shaking by hand are the same.

**Part III. Comparison of the Microstructures in Extremely Dilute Solutions to Those in Concentrated Solutions.** To compare the microstructures in concentrated solutions, we show the FF-TEM micrographs of the  $L\alpha$ -phase at rest and after shaking at 100 mM  $C_{14}$ DMAO, 30 mM Texapon N<sub>70</sub>, and 30 mM methylformate<sup>28</sup> in Figure 16 (parts a and b). Figure 16a shows a micrograph of the  $L\alpha$ -phase formed after the completion of hydrolysis of methylformate without shaking. One can observe the typical pattern for the stacked bilayer of the normal  $L\alpha$ -phase. This micrograph thus clearly shows that the combination of anionic surfactant and cationic surfactant formed by the protonation from zwitterionic surfactant ( $C_{14}$ DMAO) in the  $L_1$ -phase in the absence of shearing forces leads to a normal  $L\alpha$ -phase and not to a vesicle phase. Figure 16b shows that the vesicles were produced by shear. Obviously, the vesicle phases have been produced from the normal  $L\alpha$ -phase by shearing forces in the shaking procedure. The FF-TEM results of the two samples clearly demonstrated that the generally held assumption that stable vesicles formed spontaneously in catanionic surfactant mixtures may be the result of shearing forces that occur during the mixing process of the two components.

As opposed to the vesicles produced by chemical reaction in extremely dilute solutions, the stacked bilayer  $L\alpha$ -phase might be formed by chemical reactions in the concentrated solutions and the classic bilayer  $L\alpha$ -phase could be transferred into vesicles by shearing forces. Thus, vesicle formation depends on the conditions. At lower concentration, vesicle formation does spontaneously occur, and the resultant vesicle phase is a thermodynamically stable state. In concentrated solutions, however, vesicle formation does not spontaneously occur, but vesicles could be prepared by shearing forces, that is, the shearing forces might be responsible for the formation of vesicles.

## Conclusion

To conclude, true spontaneous vesicle formation by developing the extremely dilute aqueous catanionic surfactant mixtures

by a kinetic reaction without shear forces is achieved and characterized for the first time. The result should play an important role in the fundamental understanding of the relationship between self-assembled microstructures and external factors such as shear forces.

**Acknowledgment.** This work was supported by the NFSC (20243007), the Alexander von Humboldt Foundation, the Program of Hundreds Talent of the Chinese Academy of Sciences, and Shandong University (J.H.) and by the NSFC (50275142) and MST (2202AA302609) (W.L.).

## References and Notes

- (1) Kaler, E. W.; Murthy, A. K.; Rodriguez, B. E.; Zasadzinski, J. A. *N. Science* **1989**, *245*, 1371–1374.
- (2) Spontaneous Equilibrium Surfactant Vesicles. U.S. Patent 5, 1994, 165.
- (3) Kaler, E. W.; Herrington, K. L.; Murthy, A. K.; Zasadzinski, J. A. *N. J. Phys. Chem.* **1992**, *96*, 6698.
- (4) Herrington, K. L.; Kaler, E. W.; Miller, D. D.; Zasadzinski, J. A.; Chiruvolu, S. *J. Phys. Chem.* **1993**, *97*, 13792.
- (5) Yacilla, M. T.; Herrington, K. L.; Brasher, L. L.; Kaler, E. W.; Chiruvolu, S.; Zasadzinski, J. A. *J. Phys. Chem.* **1996**, *100*, 5874.
- (6) Jung, H. T.; Coldren, B.; Zasadzinski, J. A.; Iampietro, D. J.; Kaler, E. W. *PNAS* **2001**, *98*, 1353.
- (7) Dubois, M.; Deme, B.; Gulik-Krzywick, B.; Dedieu, J. C.; Vautrin, C.; Desert, S.; Perez, E.; Zemb, Th. *Nature* **2001**, *411*, 672.
- (8) Zemb, Th.; Dubois, M.; Deme, B.; Gulik-Krzywick, B. *Science* **1999**, *283*, 816.
- (9) Dubois, M.; Dedieu, J. C.; Deme, B.; Gulik-Krzywick, B.; Zemb, Th. *Supramolecular Structure in Confined Geometries*; ACS Symposium Series 736; Manne, S., Warr, G. G., Eds.; ACS: Washington, DC, 1999; Chapter 6, pp 86–101.
- (10) Dubois, M.; Zemb, Th. *Langmuir* **1991**, *7*, 1352.
- (11) Marques, E. F.; Regev, O.; Khan, A.; Miguel, M. G.; Lindman, B. *Macromolecules* **1999**, *32*, 6626.
- (12) Marques, E. F.; Regev, O.; Khan, A.; Miguel, M. G.; Lindman, B. *J. Phys. Chem. B* **1998**, *102*, 6746.
- (13) Edlund, H.; Sadaghiani, A.; Khan, A. *Langmuir* **1997**, *13*, 4953.
- (14) Caria, A.; Khan, A. *Langmuir* **1996**, *12*, 6282.
- (15) Marques, E.; Regev, O.; Edlund, H.; Khan, A. *Langmuir* **2000**, *16*, 8255.
- (16) Hoffmann, H.; Kalus, J.; Schwander, B. *Ber. Bunsen-Ges. Phys. Chem.* **1987**, *91*, 99.
- (17) Tamori, K.; Kihara, K.; Sanda, H.; Esumi, K.; Meguro, K.; Thunig, C.; Hoffmann, H. *Colloid Polym. Sci.* **1992**, *270*, 885.
- (18) Kawasaki, H.; Imaahayashi, R.; Tanaka, S.; Almgren, M.; Karlsson, G.; Maeda, H. *J. Phys. Chem. B* **2003**, *107*, 8661.
- (19) Villeneuve, M.; Kaneshina, S.; Imae, T.; Aratono, M. *Langmuir* **1999**, *15*, 2029.
- (20) Keller, S. L.; Boltenhagen, P.; Pine, D. J.; Zasadzinski, J. A. *Phys. Rev. Lett.* **1998**, *80*, 2725.
- (21) Helfrich, W.; Winterhalter, M. *J. Phys. Chem.* **1992**, *96*, 327.
- (22) Oberdisse, J.; Couve, C.; Appell, J.; Berret, J. F.; Liguore, C.; Porte, G. *Langmuir* **1996**, *12*, 248.
- (23) Safran, S. A.; Princus, P.; Andelman, D. *Science* **1990**, *248*, 354.
- (24) Laughlin, R. G. *Colloid Surf. A* **1997**, *128*, 38.
- (25) Lasic, D. *J. Colloid Interface Sci.* **1990**, *140*, 320.
- (26) Bergmeier, M.; Hoffmann, H.; Thunig, C. *J. Phys. Chem. B* **1997**, *101*, 5767.
- (27) Horbaschek, K.; Hoffmann, H.; Hao, J. *J. Phys. Chem. B* **2000**, *104*, 2781.
- (28) Hao, J.; Hoffmann, H.; Horbaschek, K. *J. Phys. Chem. B* **2000**, *104*, 10144.
- (29) Hao, J.; Hoffmann, H.; Horbaschek, K. *Langmuir* **2001**, *17*, 4151.
- (30) Keiderling, U.; Wiedenmann, A. *Physica B* **1995**, *213–214*, 895.
- (31) Chen, S. H.; Lin, T. L. *Methods Exp. Phys.* **1987**, *23B*, 489.
- (32) Keiderling, U. *Physica B* **1997**, *234–236*, 1111.
- (33) Zana, R. *Surfactant Solutions—New Methods of Investigation*; Marcel Dekker Inc.: New York and Basel, 1987.
- (34) Provencher, S. W. *Biophys. J.* **1976**, *16*, 27.
- (35) Provencher, S. W. *J. Chem. Phys.* **1976**, *64*, 2772.
- (36) Rathman, J. R.; Christian, S. D. *Langmuir* **1990**, *6*, 391.